Heliyon 6 (2020) e05358

Contents lists available at ScienceDirect

Heliyon

journal homepage: www.cell.com/heliyon

Case report

Decision-level fusion of Sentinel-1 SAR and Landsat 8 OLI texture features for crop discrimination and classification: case of Masvingo, Zimbabwe

Shengbo Chen [a,**], Juliana Useya [a,b,*], Hillary Mugiyo [c,d]

[a] College of GeoExploration Science and Technology, Jilin University, Changchun, 130026, China
[b] Department of Geomatics Engineering, University of Zimbabwe, 630 Churchill Avenue, Harare, Zimbabwe
[c] Ministry of Lands, Agriculture & Rural Resettlement, Zimbabwe
[d] School of Agricultural, Earth and Environmental Sciences, University of KwaZulu-Natal, South Africa

ARTICLE INFO

Keywords:
GLCM
Texture feature
Decision-level fusion
Speckle filtering
Crop discrimination
Agricultural engineering
Atmosphere modelling
Earth-surface processes
Environmental analysis
Environmental assessment
Remote sensing
Sustainable development

ABSTRACT

Radar imagery have few polarization bands which can limit the ability to do traditional digital classification. Harmonization of Sentinel-1 and Landsat 8 data despite having complementary texture information can be a challenge. The objectives of this paper are to explore texture features derived from Landsat 8 OLI and dual-polarized Sentinel-1 SAR speckle filtered and unfiltered backscatter, to aggregate classification results using Decision-Level Fusion (DLF), and to evaluate the performance of decision-level fused maps. Gray Level Co-occurrence Matrix (GLCM) is employed to derive sets of seven texture features for Landsat 8 bands and VV + VH backscatter using 5 × 5, 7 × 7, 9 × 9, and 11 × 11 window sizes. Each texture feature is stacked with a respective source image and classified using Support Vector Machine (SVM). Classified maps from the best three performers from both speckle filtered and unfiltered are aggregated with classified maps from Landsat 8 using plurality voting algorithm and compared using Z-test. Results indicate an overall classification accuracy of 96.02% from DLF images of Landsat and non-speckle filtered maps, whereas Landsat and speckle filtered achieved 94.69%. The best texture information are derived from the blue band followed by the red band, whereas speckle unfiltered textures performed better than speckle filtered textures. We conclude that integration of Landsat 8 and Sentinel-1, either speckle filtered or unfiltered, improves crop classification and speckles do not have statistically significant effects ($p = 0.1208$).

1. Introduction

The world is generally inundated by a spatial data spectrum ranging from imagery (satellite and aerial) to airborne LiDAR to crowdsourced data [1]. Numerous airborne and satellite-borne sensor systems are availing remote sensing data to the community in varying spatial and temporal scales. The utilization of agricultural remote sensing technology has been on the rise and has introduced a new dimension in enhancing agricultural systems globally [2]. There is a noteworthy increase in the diversity of applications and the scope of crop discrimination techniques that are constantly developing the remote sensing theory and the technological tools [3]. Crop type discernment is usually an imperative stage in the management and development of crop monitoring systems [3, 4].

Sundry sensors have been manufactured with optical or microwave or thermal regions of the electromagnetic spectrum and introduced new opportunities for studying within-field variations [2]. Optical data have demonstrated to be beneficial to the crop discrimination but oftentimes inescapable clouds throughout the planting season are one of the primary sources of noise, hence complicating the acquisition of valuable data on an operational basis [5]. All-weather capabilities of radar systems have immensely helped overcome the inescapable cloud problem. Accordingly, Synthetic Aperture Radar (SAR) is the most active sensor for microwave data [3].

Spaceborne radar data are affected by the presence of speckles and fewer polarization bands [6] thereby reducing the capacity to perform traditional digital classification. Textural and tonal features are obtainable when SAR images are independently processed on a computer [7, 8]. Gray tone on its own in SAR images has proved to have a minimal ability

* Corresponding author.
** Corresponding author.
E-mail addresses: chensb@jlu.edu.cn (S. Chen), julieuseya@yahoo.co.uk (J. Useya).

https://doi.org/10.1016/j.heliyon.2020.e05358
Received 28 May 2020; Received in revised form 21 August 2020; Accepted 23 October 2020

in discriminating land-cover classes [9], but the texture is one crucial attribute of radar that can expedite in obtaining correct surface information [10].

Texture is a key cue employed in visual interpretation such that texture descriptors can upsurge the performance of digital classification algorithms. It can probably be more valuable than image tone when interpreting radar images [5]. Tone and texture are disparate object properties, spectral and spatial are very likely to be independent data but complement one another. Texture features are intricate visual patterns comprising of sub-patterns or entities which contain attributes such as color, brightness, size, slope, etc. [11]. One advantage of texture is that it does not alter with respect to light. Kappa coefficient from crop discrimination algorithms tends to improve as more bands and polarizations are added [12]. The Kappa measurement indicates the variation between the actual agreement and the agreement expected by chance.

According to Materka & Strzelecki [13], approaches to texture analysis are usually categorized into structural approaches, statistical approaches, model-based approaches and transform. In statistical textual analysis, texture features can be calculated from the statistical distribution of observed combinations of intensities at specified positions relative to each other in the image. There are various methods used as measures for the textural description of images which include first-order, second-order, and higher-order statistical methods. Haralick et al. [14] proposed the utilization of Gray Level Co-occurrence Matrices (GLCM) that have become popular and extensively used texture features [3, 15]. This research is implementing the GLCM features.

The GLCM functions illustrate the texture characteristics of an image by computing the frequency of pairs of pixels with explicit values and in a specified spatial relationship occur in an image, generating a GLCM, and then extricating statistical measures from this matrix [16, 17]. The local sub-patterns in one calculation engender the apparent linearity, lightness, smoothness, coarseness, uniformity, regularity, roughness, frequency, phase, directionality, density, fineness, randomness, granulation, etc., of the texture as a whole [11, 13, 18, 19, 20].

Crop discrimination capability of SAR data can be enhanced by utilizing speckle filters which are based on local statistics [5, 21, 22]. Lee et al. [23] provided an in-depth review of numerous speckle filtering algorithms existing in the literature. On the other hand, speckle reduction can result in some loss of texture information, and problems can emanate from small fields [5]. According to Ulaby et al. [24] and Soares et al. [5], speckle is considered to be autonomous of the textural disparities linked with the spatial associations of the scattering properties of distributed targets. According to Lopes et al. [25], the speckle is lessened as a function of the heterogeneity observed by the local coefficient of variation. Speckle filtering can be less effective when the radar backscatter is subjected to substantial disparities due to the existence of rugged scatterers or structural features (edges or lines) in the processing window [25]. Nonetheless, speckle filtering can obliterate backscatter texture at scales near that of the resolution cell [26]. The principal question requiring more research is whether speckle filtering to be applied if texture features are to be utilized for land cover/use classification [10].

Suitable optical image spectral bands can also be utilized to derived texture features and when appended with spectral data as input variables [20] can enhance crop discrimination. Nevertheless, when a large number of texture features and spectral bands are combined, it can result in high data dimensionality which can require a highly suitable computational statistical algorithm [20]. Classification of such can be time-consuming as well. On the other hand, according to Forget et al. [27], Landsat 8 and Sentinel-1 contain some complementary information that can be exploited for classification benefits. The challenge is how to merge the complementary information to fully exploit the valuable information from both sensors.

Decision-level fusion combines individual classification results into a single seamless map. There is no prior knowledge regarding the band configuration of sensors required for decision-level fusion [28]. Endeavoring to limit/minimize the feature vector, this research will append only one texture feature with either Landsat 8 bands or VV + VH backscatter of Sentinel-1 at a time. Decision-level fusion allows the integration of the respective classified results in a simple way. Various existing algorithms can be implemented which include majority voting, decision templates, Dempster-Shafer, Borda count, and many more [27].

Spatially explicit information about crop types has both a direct and indirect impact on crop area estimation, crop yield forecasting, etc. At a global level, comprehensive crop yield and crop extent data can assist in ascertaining where investment from major donors can be very beneficial in terms of enhancing agricultural output. At a regional level, detailed information can be utilized to assist in understanding the effects of drought and other natural and manmade disasters on food production [29]. At both national and sub-national levels, correct information regarding cropland can further be employed to detect trends in agricultural outputs and to determine if investments have led to the expected results.

Zimbabwe generally lacks updated spatially explicit information regarding the crop type distribution inventory system. As determined by Hentze et al. [30], there is an alleged deficiency of precise and spatially explicit approaches to derive independent and objective information pertaining to the extent of agricultural areas in Zimbabwe. The previous research on crop type mapping [31, 32, 33] have utilized MODIS NDVI imagery that has a coarse spatial resolution of 250 m, henceforth, limits its ability to depict small and heterogeneous farms. Zimbabwe cropland comprises small, fragmented farm fields that cannot be reliably depicted from coarse spatial resolution imagery.

Due to the increase in the availability of free imagery from multiple sensors with relatively high spatial resolution and possess complementary information to benefit the classification results, but may have different band configurations or when stacked can produce high data dimensionality. The objectives of this paper are to (i) explore GLCM texture features derived from Landsat 8 OLI and dual-polarized Sentinel-1 SAR speckle filtered and unfiltered backscatter under varying window sizes; (ii) apply decision-level fusion to aggregate classification results for enhanced crop discrimination; (iii) assess the performance of decision-level fused maps.

2. Materials and methods

2.1. Study area

The area under study is in Masvingo province, which is situated in the south-east of Zimbabwe. The province shares boundary with Mozambique in the eastern part and Matabeleland South province is to the southern part, Midlands province is to the north and west part, whereas, Manicaland province to the north-east part [34]. It has an area of 56,566 km^2, approximately 14.48% of the total area of Zimbabwe. Zimbabwe experiences a bimodal rainfall pattern and it has three distinct seasons namely: (i) a wet and hot season from mid-November to March (summer); (ii) a dry and cold, season from April to July (winter); and (iii) a dry and hot season from August to mid-November (spring). The average winter temperatures are between 15 °C and 20 °C and summer average temperatures are between 25 °C and 30 °C.

It is situated in the Lowveld with an altitude below 900 m, and agro-ecological regions III, IV, and V with a very low mean rainfall of below 600 mm in the Save-Limpopo valley. The rainfall pattern of the area is erratic hence not reliable for the production of grain crops and drought-tolerant fodder. The district experiences frequent dry spells and droughts throughout the rainy season. Therefore, farming has to be centered on the use of veld alone. The extensive cattle ranching or game ranching is the only sounding farming system for this region. Land reform program implemented in Zimbabwe since 1980 led to an agrarian structure accounting for up to 98% small-scale farms of the total agriculture land [34].

2.2. Datasets

2.2.1. Training, testing, and validation samples

Samples (training, testing, and validation) were collected by hand-held GNSS receivers (Trimble Juno 5d, Garmin etrex 10, etrex Vista, and etrex 20) during the crop growing season (January and March 2018). UTM coordinate system using WGS84 ellipsoid was adopted during the field campaigns. Appendix 1 shows some of the images for the sample locations (as shown in Figure 1) taken during the fieldwork. Each class had a minimum of 75 points (50 are used for training and 25 are used for validation). In total, a minimum of 1000 points was acquired.

2.2.2. Sentinel-1 SAR

The European Space Agency (ESA) launched a constellation of two polar-orbiting radar satellite Sentinel-1A and 1B in April 2014 and April 2016 respectively. It operates during the day and night providing singular and dual-polarimetric, multi-temporal, C-band synthetic aperture radar (SAR) imaging data. The data is freely accessible to all users. It can acquire images with varying processing levels in three acquisition modes namely: Wave (WV), Interferometric Wide Swath (IW) Extra Wide Swath (EW), and Stripmap (SM) [35].

For this research, from the Sentinel data hub, https://scihub.copernicus.eu/ website, Ground Range Detected (GRD) Sentinel-1 C-band (5.405 GHz) Level-1 images in Interferometric Wide swath (IW) mode are downloaded. The IW mode enables the merging of a wider swath width (250 km) with a moderate geometric resolution (10 m). The GRD products comprise intensity and amplitude images in each polarization (VV and/or VH) with Level-1 processing that consists of data projected to ground range utilizing an earth ellipsoid model, thermal noise removal, elevation antenna pattern, and range spreading loss corrections [36]. The IW image with incidence angle ranging from 30° to 45° and a pixel spacing of 10 m in both azimuth and range. Table 1 illustrate the acquisition dates of images implemented.

2.2.3. Landsat 8 OLI

2 scenes of Landsat 8 Level-1, acquired on the 26th of April 2018 with path/row: 169/74 and 169/75 are downloaded from https://earthexplorer.usgs.gov which are mosaicked after pre-processing.

2.3. Methodology

2.3.1. Generic flowchart

Figure 2 shows the generic flowchart illustrating processes followed in the implementation of this research. Image acquisition is the first step, followed by preprocessing, then texture image extraction. Each texture image is stacked with respective source images and classified using the Support Vector Machines (SVM) algorithm. The best three performing input variables from Sentinel-1 are aggregated with the best three performing variables from the Landsat 8 variables. The approach adopted in this paper is in three main parts:

- Derivation of .GLCM textural features from Sentinel-1 speckle filtered backscatter.
- Ignoring the speckle and apply GLCM to create the textural features from Sentinel-1 backscatter.
- Derivation of GLCM textural features from Landsat 8 spectral bands.

All the processes in the flowchart are explained in the following subsections from 2.3.2 to 2.9.

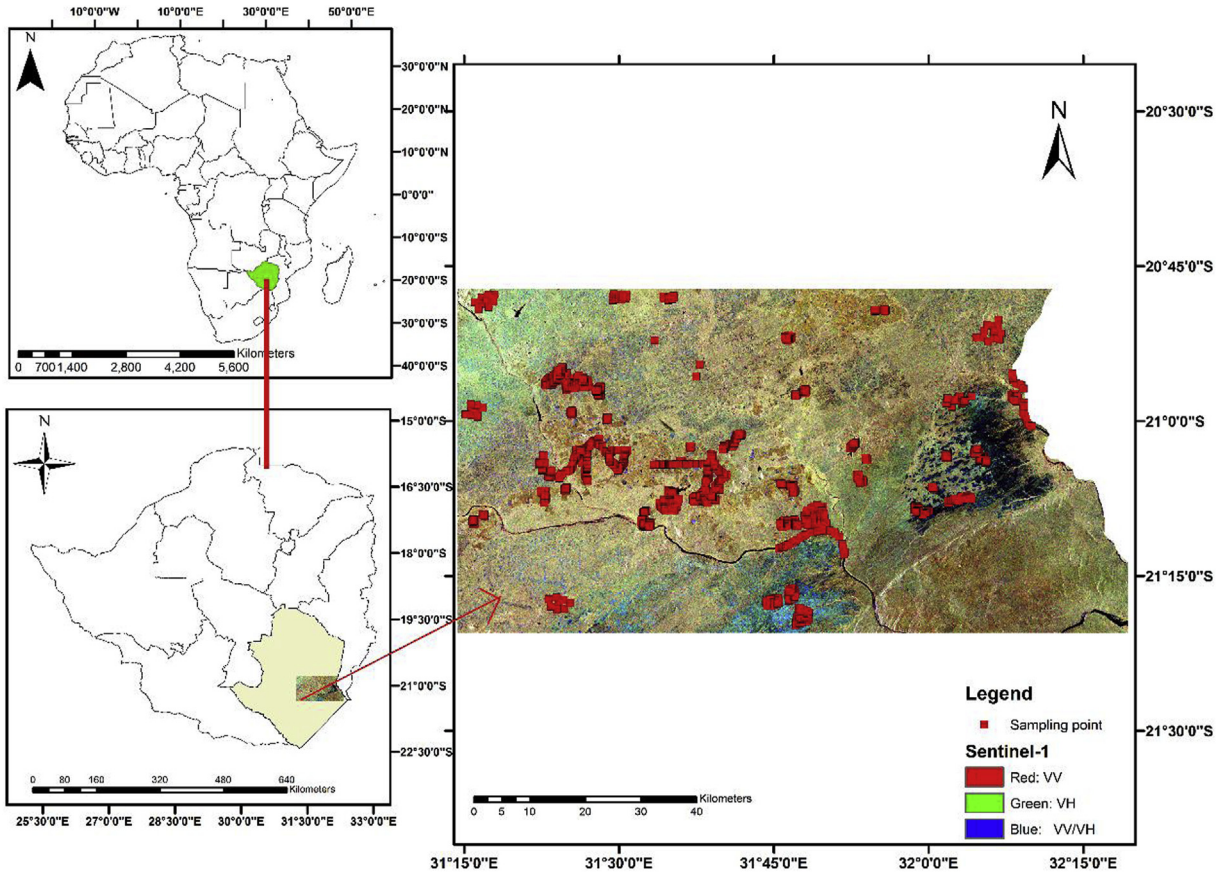

Figure 1. The study site located in Masvingo Province of Zimbabwe.

Table 1. Name and characteristics of Sentinel-1 SAR and Landsat 8 OLI images acquired.

Product	Acquisition Date	Characteristics
Sentinel-1..	15 April 2018	Data product: Level-1 GRD Imaging mode: IW Imaging frequency: C-band (5.405 GHz) Polarization: VV and VH
Sentinel-1	22 April 2018	
Landsat 8	26 April 2018	Path/row: 169/74 and 169/75 Level 1

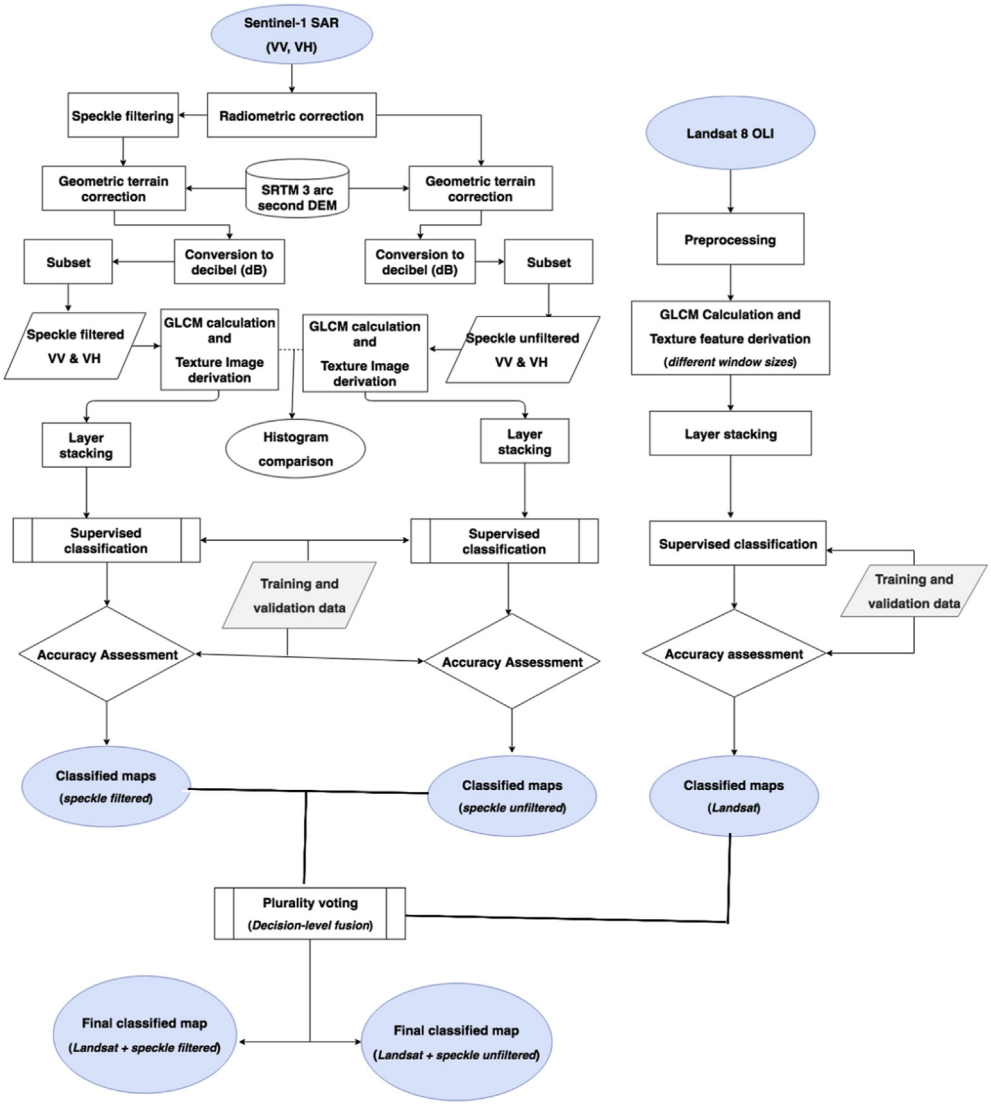

Figure 2. Generic flowchart for GLCM texture feature extraction, classification, and integration.

2.3.2. Sentinel-1 preprocessing

The image is quantized to a level of 32 bits pixel to reduce computation time and minimize memory requirements. The acquired images are radiometrically corrected but only one set is speckle filtered, then the other set, no speckle filtering is applied. The pre-processing is completed by applying the geometric terrain correction and conversion of backscatter to decibel, then clipping off the pre-processed images to the size of the study site. The atmosphere and terrain undulations can affect the radiometric and geometric quality of SAR imagery [37]. Radiometric correction refers to enhancing the interpretability and quality of information contained by the SAR imagery. The radiometric correction is essential to correct the distortions due to the effects of atmosphere and topography. Geometric terrain correction refers to the compensation of distortions on the geometric quality due to the effects of terrain. It is achieved by utilizing SRTM 3 arc-second DEM. The geometric correction is crucial to ensure that the x, y location of each pixel lies in the correct geographic location.

Seven texture features for each dataset are calculated and synthesized using ESA's SNAP 6.0, Sentinel-1 toolbox utilizing probabilistic quantizer, an average of all angles (0º, 45º, 90º, 135º), and window sizes 5×5, 7×7, 9×9 and 11×11. SAR texture feature classification accuracy is greatly affected by the window size, hence the choice of window size

requires careful consideration [38]. Stable texture features result usually from bigger windows but they have a tendency to blur the edges, whereas smaller windows tend to inaccurately delineate boundaries and misclassify the boundaries [38].

Sets of seven texture feature images are synthesized from VH and VV polarized backscatter for the Sentinel-1 SAR images acquired (both speckle filtered and unfiltered). The seven texture features derived are (a) ASM (b) contrast (c) dissimilarity (d) entropy (e) homogeneity (f) mean (g) variance. A total of 224 texture features are created, which is 112 for speckle filtered and 112 for speckle unfiltered datasets.

2.3.3. Landsat 8 OLI pre-processing

The downloaded scenes are radiometrically corrected, then atmospherically corrected and mosaicked. Polygon of the study area is used to clip the pre-processed image.

Seven GLCM texture features from each of the following spectral bands are derived: blue, red, green, NIR, SWIR1, and SWIR2 with an average of all angles (0º, 45º, 90º, 135º) and window sizes: 5 × 5, 7 × 7, 9 × 9 and 11 × 11 with 32-bit quantization level of the output channel. The seven texture features derived are (a) ASM (b) contrast (c) dissimilarity (d) entropy (e) homogeneity (f) mean (g) variance. A total of 168 features are created.

2.3.4. GLCM textural features

Texture features are calculated from the statistical dispersion of observed combinations of intensities at unique locations relative to each other in the image [39]. Shanmugan et al. [7] defined the second-order GLCM of an image.

Haralick et al. [14] proposed 14 texture measures. Texture measures are the various single values used to summarize the normalized symmetrical GLCM in helpful ways [40]. The majority of texture computations are weighted means of the normalized GLCM cell contents [40]. GLCM textural features derived for this research are as follows:

a. Contrast (also called "sum of squares variance" and occasionally "inertia"

$$\sum_{i,j=0}^{N-1} P_{i,j}(i-j)^2 \tag{1}$$

b. Dissimilarity

$$\sum_{i,j=0}^{N-1} P_{i,j}\left|i-j\right| \tag{2}$$

c. Homogeneity (Inverse Difference Moment)

$$\sum_{i,j=0}^{N-1} \frac{P_{i,j}}{1+(i-j)^2} \tag{3}$$

d. Angular Second Moment (ASM)

$$\sum_{i,j=0}^{N-1} P_{i,j}^2 \tag{4}$$

e. Entropy

$$\sum_{i,j=0}^{N-1} P_{i,j}\left(-InP_{i,j}\right) \tag{5}$$

f. GLCM Mean

$$\mu_i = \sum_{i,j=0}^{N-1} i\left(P_{i,j}\right) or\, \mu_j = \sum_{i,j=0}^{N-1} j\left(P_{i,j}\right) \tag{6}$$

g. Variance (Standard Deviation)

$$Variance\ \sigma_i^2 = \sum_{i,j=0}^{N-1} P_{i,j}(i-\mu_i)^2 or\ \sigma_j^2 = \sum_{i,j=0}^{N-1} P_{i,j}\left(j-\mu_j\right)^2 \tag{7}$$

2.4. Histogram comparison

A histogram shows the statistical frequency of data distribution in a dataset. It is essential to understand the distribution of the dataset we are working with, whether it is normally distributed, how skewed it can be, and determine outliers. There is no right or wrong way of determining the width of a bin (class intervals), though there are rules of thumb that exist. Lane [35] explained the *Sturges' rule* which states that the number of intervals can be set as close as possible to 1 + Log2(N), where Log2(N) is the base 2 log of the number of observations. Rice rule, sets the number of intervals to twice the cube root of the number of observations [41] There is also the Freedman-Diaconis rule, which seems very robust and works well in practice.

Histograms are tools regularly used in object recognition, image classification, image retrieval, and shape matching, to represent color and texture features or to distinguish rich information in local/global regions of objects [42]. A commonly used technique in data analysis is the comparison of histograms that is to compare histograms of one image with another to determine if the images are approximately the same or not. An important task in histogram comparison is testing their compatibility or testing their distinguishability [43]. Comparison of the histogram of grayscale images can be: (i) Horizontal Mirrored histograms or (ii) Vertical Mirrored Histogram or (iii) Overlaid histograms. This research utilizes MATLAB to implements the overlaid histograms method. Spatially enhanced histogram can be exploited further when defining the distance measure [44].

2.5. Texture feature image classification

SVM is an extensively used non-parametric statistical machine learning algorithm that is predominantly alluring in the remote sensing field due to its capacity to effectively deal with small training samples, frequently resulting in better classification accuracy than the traditional methods [35, 45, 46]. The principle of SVM is to define an optimum hyperplane to maximize margin width by using a training subset [35, 46]. An optimal separating hyperplane refers to the decision boundary that lessens misclassifications attained during the training step [46]. Boser et al. [47] proposed a way to create nonlinear classifiers by applying the kernel trick to maximum-margin hyperplane [42, 48]. He et al. [42] gave detailed information regarding the SVM algorithm. The SVM algorithm is chosen due to some of its advantages which include being fast and that they possess a satisfactory capability to deal with crop classification problems [28].

The SVM classification method is implemented for the crop discrimination and mapping of texture images created from window sizes 5 × 5, 7 × 7, 9 × 9, and 11 × 11. Each texture feature is stacked with respective source imagery prior to classification and are presented as follows: (i) Speckle filtered texture feature + (VV + VH); (ii) Non-speckle filtered texture feature + (VV + VH) and (iii) texture feature + Landsat 8.

2.6. Classification accuracy assessment

To evaluate the performance of the SVM classification algorithm on the datasets under investigation, confusion/error matrices are employed. Error matrix is one standard technique implemented to evaluate the accuracy of classification in remote sensing. It summarizes the performance of a classification algorithm by comparing the classified land use with ground truth data and computes overall accuracy, kappa coefficient, producer's and user's accuracies [49], and commission and omission errors. The field data utilized in this paper is split into 60% training and 40% for evaluation.

2.7. Resampling

Resampling is a procedure where different pixel values are computed using interpolation from old existing values each time the raster's structure is altered throughout the cell modification process [44]. Imagery from various sensors require resampling such that the registration is precise and correct to subpixel locations [51]. Before decision-level fusion, a classified map from Landsat 8 texture variables have a spatial resolution of 30 mpp, whereas classified images from Sentinel-1 texture variables have 10 mpp spatial resolution. Sentinel-1 classified images are resampled to 30 mpp to match Landsat's. Nearest neighbour (NN) interpolation resampling algorithm is executed in ArcMap aimed at reducing data integrity losses due to the cell resizing since such resampling can result in substantial effects on the data integrity being compared [50]. NN is appropriate due to its capacity to maintain the integrity of categorical data and swiftness [50].

Root Mean Square Error (RMSE) is calculated and is implemented to evaluate the quality of the resampled dataset.

$$RMSE = \sqrt{\frac{\sum_{a=1}^{m}\left[\left(X_a^r - X_a\right)^2 + \left(Y_a^r - Y_a\right)^2\right]}{n}} \tag{8}$$

where $X^r_a;Y^r_a$ are coordinates of control stations on resampled image, $X_a;Y_a$ are coordinates of control stations on reference image.

An overall RMSE of is achieved 0.016 m.

2.8. Plurality voting (decision-level)

Prior to decision-level fusion, resampling is performed such that maps can have the same matching spatial resolution. The plurality voting algorithm [28] is employed to combine classified images from Landsat and Sentinel-1. It is a relatively simple method.

2.9. Z-test

According to Rossiter [52], map producers and users have to compare maps to distinguish their accuracy. Producers usually compare various classification algorithms, whereas users are normally determining better maps for a specified application. Users may require to determine two maps compare with each other. Maps can be equally accurate when considered separately, but having different errors. Depending on the intended use of maps, accuracy statistics can inform producers about the performance of classification algorithms. This paper implements Z-test to compare the relative accuracies of maps produced by the best variable combinations from the speckle filtered dataset and speckle unfiltered dataset.

3. Results

Landsat 8 texture features are classified separately from Sentinel-1 texture features (i.e. speckle filtered and speckle unfiltered). The results of best-performing textures from Landsat 8 are aggregated with best-performing texture features from Sentinel-1 speckle filtered and speckle unfiltered backscatter respectively. The performance of both resulting decision-level fusion-based classified images is compared using Z-test.

3.1. Histogram intersection

Histograms have been adopted in this research to assist in showing and discovering the underlying frequency distributions (shape) of the texture feature images implemented in this paper.

3.1.1. VV and VH texture features from speckle unfiltered images

Figure 3 shows the histogram intersection of speckle unfiltered VV and VH for all the nine texture features. There is no direct relationship between VV and VH histograms for the ASM, contrast, dissimilarity, entropy, homogeneity, mean, and variance texture features. Since GLCM equations are not normalized, the minimum and maximum values differ for each texture histogram.

Appendix 2 shows the histogram intersection of speckle filtered VV and VH texture images. The structures of the histograms are similar to those in Figure 3 for speckle unfiltered texture features.

3.1.2. Speckle filtered and non-speckle filtered VH texture features

Figure 4 shows the histogram intersection of VH texture features from the speckle filtered dataset and the other dataset is not speckle filtered. Shapes of histograms of the different corresponding texture features show some similarities. There is some form of relationship that could be developed from the histograms.

3.2. Classification performance of Landsat 8 texture features

Four window sizes (5 × 5, 7 × 7, 9 × 9, and 11 × 11) are extracted independently from red (R), green (G), blue (B), and near-infrared (NIR) bands. Figure 5 shows the top 35 performers of Landsat 8 texture features. The majority of the features within the top performers are extracted from the blue band having twenty-two, followed by red band with nine features, then both green and near-infrared have two features each. Texture information derived from the blue band worked best since they have yielded the finest characteristics about the spatial relationships of neighboring pixels which attributed to improved crop discrimination and classification accuracies.

Classification of Landsat 8 imagery (R, G, B, NIR, SWIR1, and SWIR2 bands) produced an overall accuracy of 90.37%, whereas when combined with all the textures from all the bands achieved an accuracy of 88.28% hence did not enhance the discrimination ability of the Landsat 8. Various aggregation combinations of SWIR1 and SWIR2 texture features obtained the least classification accuracies, with the highest overall accuracy of 54%. Texture features of SWIR1 and SWIR2 bands are not beneficial in the classification of crops. When having a multispectral image such as Landsat 8, it is crucial to understand the appropriate bands that contain vital texture information. Classification accuracy obtained from Landsat 8 bands together with texture features from R, G, B, and NIR is 90.14%. The observations obtained reveal that particular bands contain crucial texture information which can enhance the discrimination ability, SWIR bands have no useful texture information.

Figure 5 shows the best thirty-five textures that enhanced the crop discrimination ability of Landsat 8. Mean texture feature derived from the red band using 11 × 11 window size attained the highest accuracy of 94.39%, followed by entropy texture features extracted from the blue band using 11 × 11 window size. Fourteen texture features derived from 11 × 11 window size managed to be part of the top 35, followed by eleven features attained from 9 × 9 window size, then seven extracted using a 7 × 7 lastly only three textures gleaned from a 5 × 5 window size.

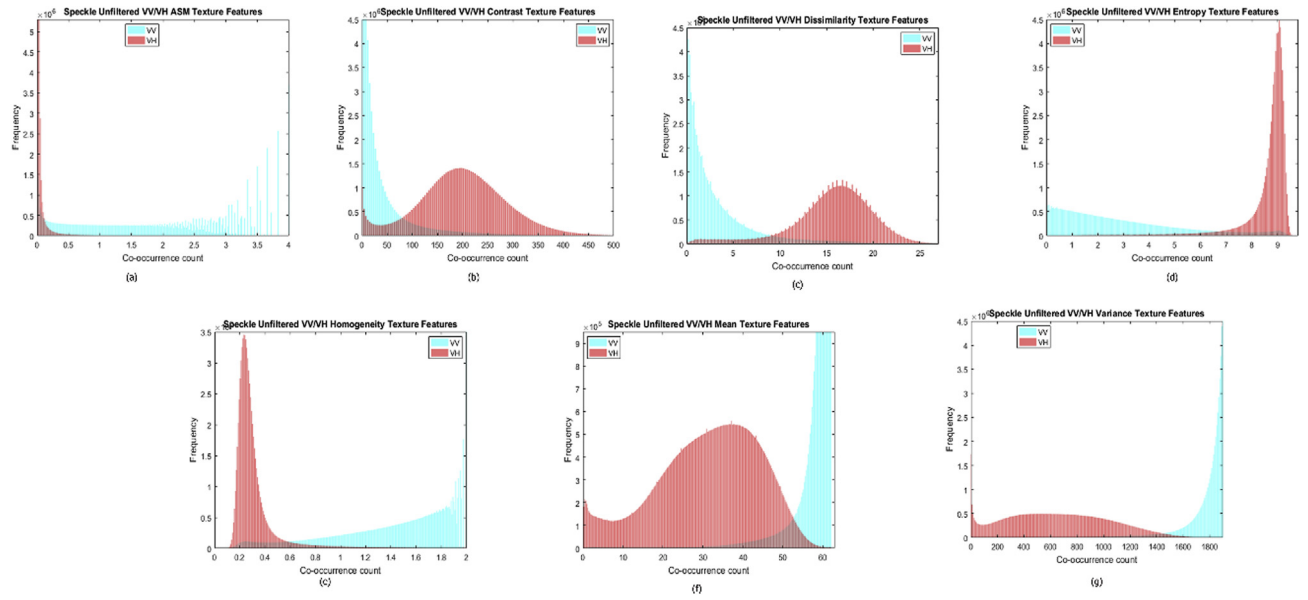

Figure 3. Histogram intersection for speckle unfiltered VV and VH texture images (a) ASM (b) Contrast (c) Dissimilarity (d) Entropy (f) Homogeneity (f) Mean (g) Variance.

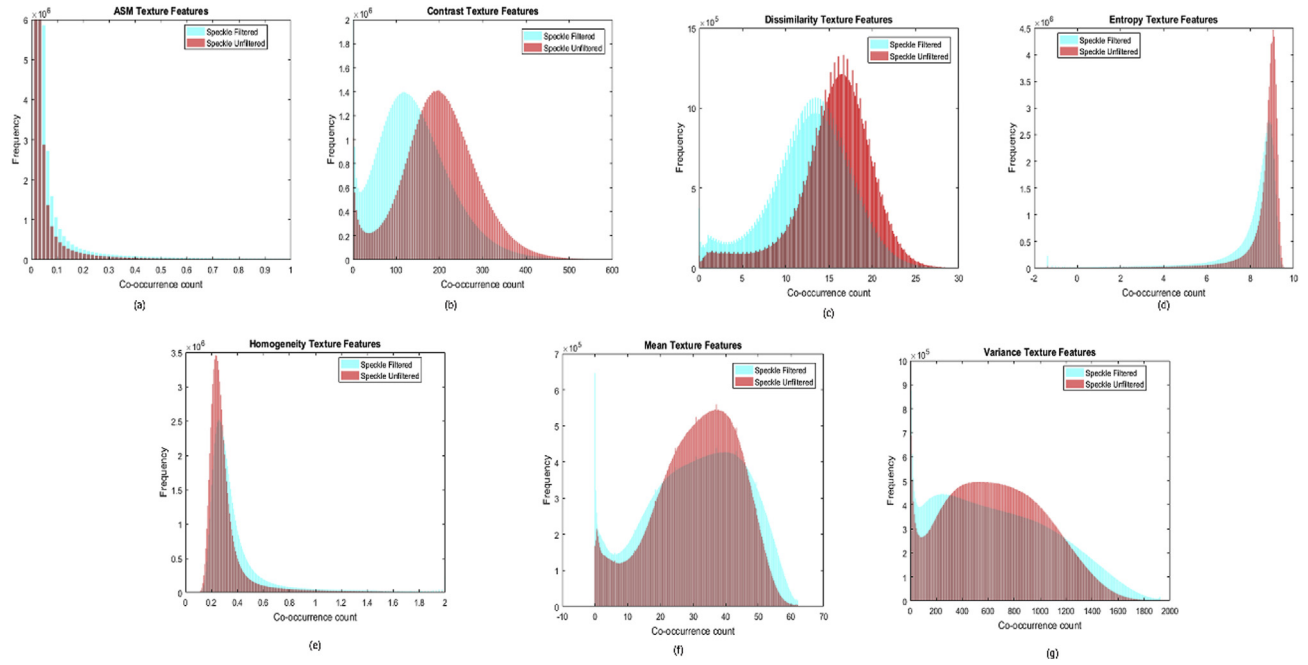

Figure 4. Histogram intersection of VH texture measures from both speckle filtered and unfiltered datasets (a) ASM (b) Contrast (c) Dissimilarity (d) Entropy (f) Homogeneity (f) Mean (g) Variance.

3.3. Classification of single polarized Sentinel-1 SAR backscatter and their corresponding texture features

VH polarimetry of Sentinel-1 SAR for the two dates attained higher accuracy of 66.90% than VV polarization which attained 58.57%. VV polarized backscatter combined with their corresponding VV texture features of both datasets are classified separately from the VH polarized counterpart variables. Appendix 3 represents the classification results obtained. VH variables outperformed VV variables, however, the addition of texture features reduced the ability of correct discrimination by single polarimetry backscatter. Contrast texture feature derived from speckle filtered backscatter from both VV and VH polarized backscatter underperformed in all case scenarios of window sizes. Discrimination ability of both single polarized backscatter combined with corresponding texture features is reduced mostly when speckle filtering is performed before texture derivation.

3.4. Classification performance of dual-polarized Sentinel-1 SAR backscatter and their corresponding texture features

Classification accuracy obtained by dual-polarized speckle filtered backscatter of Sentinel-1 is 62.11%. Sentinel-1 SAR texture features are extracted from both speckle filtered and unfiltered datasets, using 5×5, 7×7, 9×9, and 11×11 window sizes respectively. Figure 6 displays the

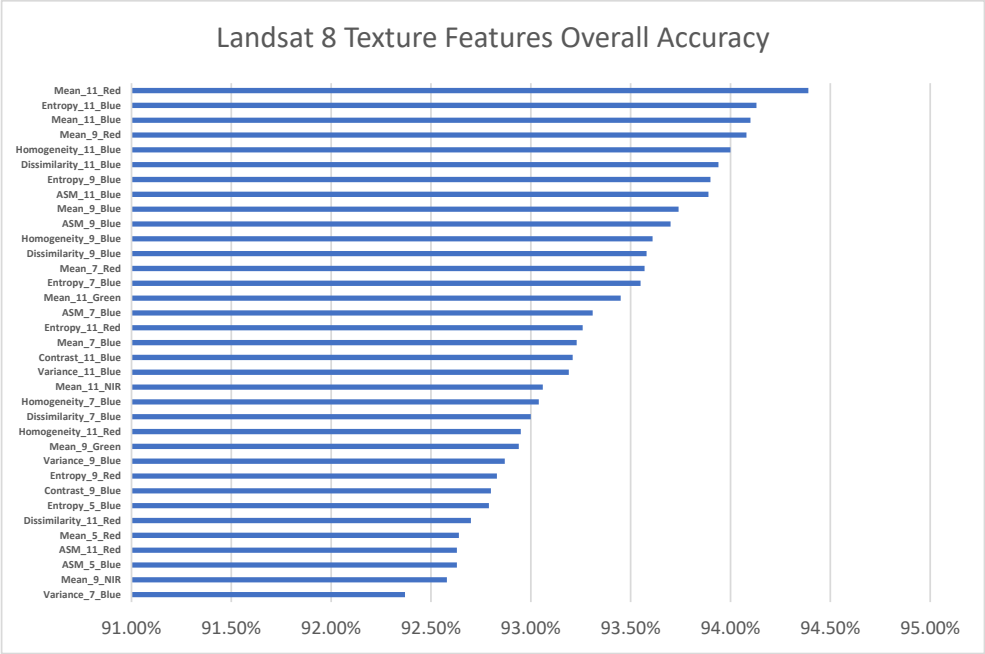

Figure 5. Overall classification accuracy of top 35 texture features stacked with Landsat 8 OLI bands 2, 3, 4, 5, 6, and 7. Mean_11_Blue means mean texture image calculated from the blue band using 11 × 11 window size.

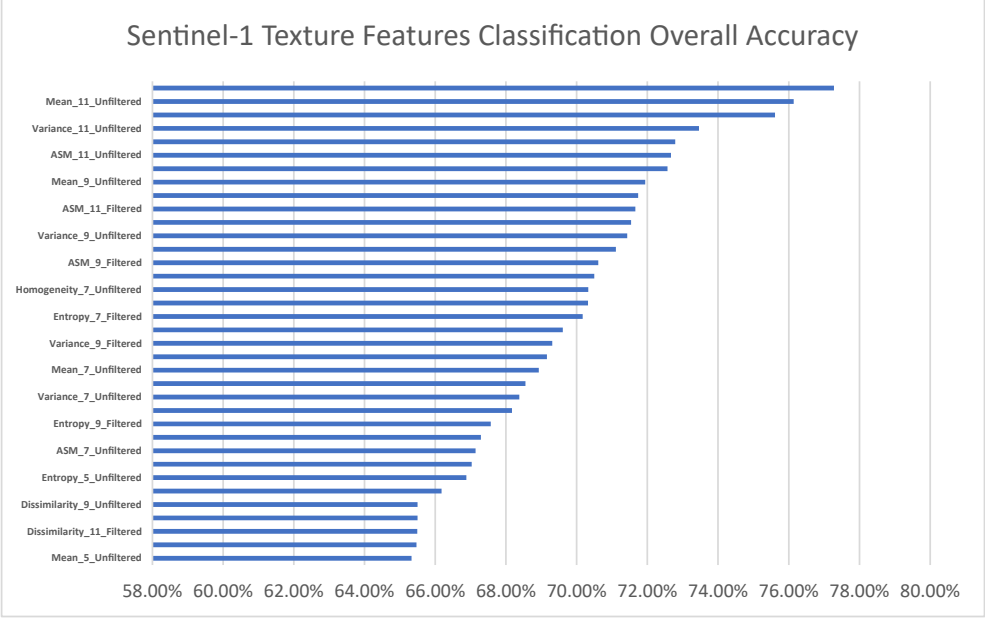

Figure 6. Overall classification accuracy of top 35 texture features stacked with Sentinel-1 VV + VH polarimetric bands. Mean_11_Unfiltered means mean texture image calculated from speckle unfiltered VV and VH bands using 11 × 11 window size.

top 35 performers of the texture features. Twenty texture features derived from the speckle unfiltered dataset are part of the top 35, whereas fifteen features computed from the speckle filtered dataset are part of the top 35 performers.

Of the texture features computed, entropy and ASM texture measures have achieved the best results having seven variables each within the top performers selected (Figure 6), six mean features followed, then five homogeneity, five variance features, four dissimilarity, and one contrast features have performed better than the others. Contrast texture features seem not to reveal the spatial relationships of neighboring pixels when compared to the other textures.

3.5. Area under the curve and receiver operating characteristic (AUC-ROC)

Evaluation of the multi-classification and visualization of the performance of the algorithm, Area Under Curve (AUC) Receiver Operating Characteristics (ROC) curves are employed. The ROC curve allows the comparison of the classifier's performance across the whole spectrum of class distributions [53]. Figure 7 illustrates the AUC-ROC curves for sugarcane, sugarbeans, cowpeas, maize, and sorghum extracted for Mean texture feature, 11 by 11 window size, Red band of Landsat 8. The AUC of sugarcane is 0.99, maize – 0.93, sugarbeans – 0.84, cowpeas – 0.79, and

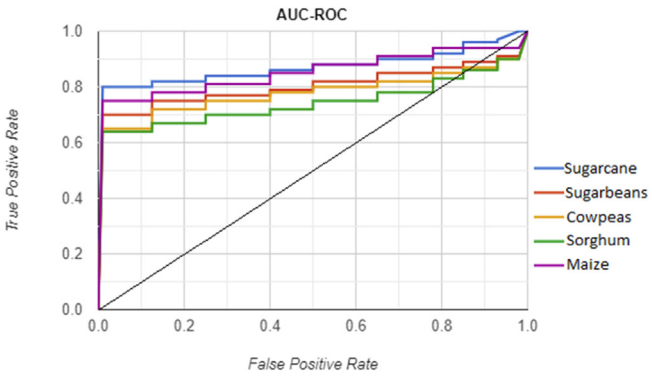

Figure 7. The Receiver Operating Characteristic (ROC), used to generate the Area Under the curve (AUC) which is used for model validation of the logistic regression model for spatial prediction of some of the crops considered. Sugarcane - 0.99, maize – 0.93, sugarbeans – 0.84, cowpeas – 0.79 and sorghum – 0.73.

sorghum – 0.73 showed the rate of successful classification by the logistic model (Figure 7). The results of AUC show the importance of ground-truthing on classification. A model has AUC which is near to the 1 which means it has a good measure of distinguishing two classes of suitability (presence and absence) [54].

3.6. Decision-level fusion results

Before decision level image fusion using the plurality voting method, an overall RMSE of 0.016 m is achieved upon resampling Sentinel-1 products to match 30 mpp of Landsat 8 products. Table 2 illustrates the overall accuracy and kappa coefficient of the respective integrated classified maps.

Figure 8 (a) depicts the final merged classified map from Landsat + Sentinel-1 speckle filtered, from window size 11 × 11. Figure 8 (b) shows the final aggregated classified map from Landsat + Sentinel-1 speckle unfiltered, from window size 11 × 11.

3.7. Z-test statistic

In remote sensing, the extensively used approach to compare classification accuracy is the comparison of kappa coefficients, the statistical significance of the variance between two autonomous kappa coefficients computed from various classifications is assessed by computing the Z-test value [47, 55]. Z-test has been performed to assess the substantial disparities between the accuracy measurements of classification results [47] from speckle filtered variables and speckle unfiltered variables.

Initial kappa coefficients are calculated in ENVI, their respective error matrices are imported in MATLAB to determine the variance estimates ($\widehat{\sigma^2_{K_1}}$ and $\widehat{\sigma^2_{K_2}}$)crucial to compare the different tests. Table 3 shows the computed z-value of 0.1208, designating that at α = 0.05, there is no significant difference between the kappa coefficients.

3.8. F1-score

Table 3 exhibits the performance evaluation of classifying both Landsat 8 + speckle filtered and Landsat 8 + unfiltered texture features using the F1-scores for each class computed from user's and producer's accuracies computed from the error matrices (accuracy assessment statistics) using Eq. (9). Since class distributions are uneven, F1-score is a harmonic mean which assists in making a robust decision on which dataset works best when classifying crop types using texture features from SAR data.

$$\text{F1} - \text{score} = 2 \times \frac{PA \times UA}{PA + UA} \tag{9}$$

where PA – producer's accuracy and UA – user's accuracy.

Speckle unfiltered + Landsat 8 performed better than speckle filtered + Landsat 8 on most classes except for maize and fallow.

Class	F1-Score of speckle unfiltered + Landsat 8 (%)	F1-Score of speckle filtered + Landsat 8 (%)
Waterbody	99.88	99.84
Sugarcane_2	97.87	97.78
Sugarcane_1	98.09	98.23
Maize	83.28	83.30
Sorghum	93.91	90.51
Sugarbean	92.22	91.91
Road/bare	76.28	75.40
Fallow	99.33	99.54
Sweet potato	88.89	87.32
No crop	97.25	97.14
Finger millet	94.49	93.90
Bambaranuts	93.91	93.52
Cowpeas	92.69	92.55
Mixed	73.65	70.49

3.9. Extracted areas

Total areas of the different classes discerned from the classification are extracted from both maps and linear regression analysis is performed. A regression coefficient R^2 of 0.9309 is achieved (Figure 9), assuming that there is a strong correlation between the two datasets.

3.10. F-test for regression

F-test has been implemented to assess the statistical significance of the relationship between the extracted areas of the different cases from the two variables. A significant F-value designates the suitability of the linear regression model. It is calculated using Eq. (10).

$$F = \frac{MSM}{MSE} \tag{10}$$

where MSM is the mean of squares of the model, MSE is the mean of squares of error.

Table 2. Overall classification accuracies and kappa coefficients of Landsat + Sentinel-1 datasets.

Output name	Classified maps	OA	KC
Landsat 8		90.37%	0.8833
Sentinel-1		62.11%	0.5986
Landsat 8 + Sentinel-1 speckle unfiltered	Homogeneity_11_Filtered +Mean_11_Filtered + ASM_11_Filtered +Mean_11_Red + Entropy_11_Blue +Mean_11_Blue	94.69%	0.9378
Landsat 8 + Sentinel-1 speckle filtered	Entropy_11_Unfiltered +Mean_11_Unfiltered + Homogeneity_11_Unfiltered +Mean_11_Red + Entropy_11_Blue +Mean_11_Blue	96.02%	0.9515

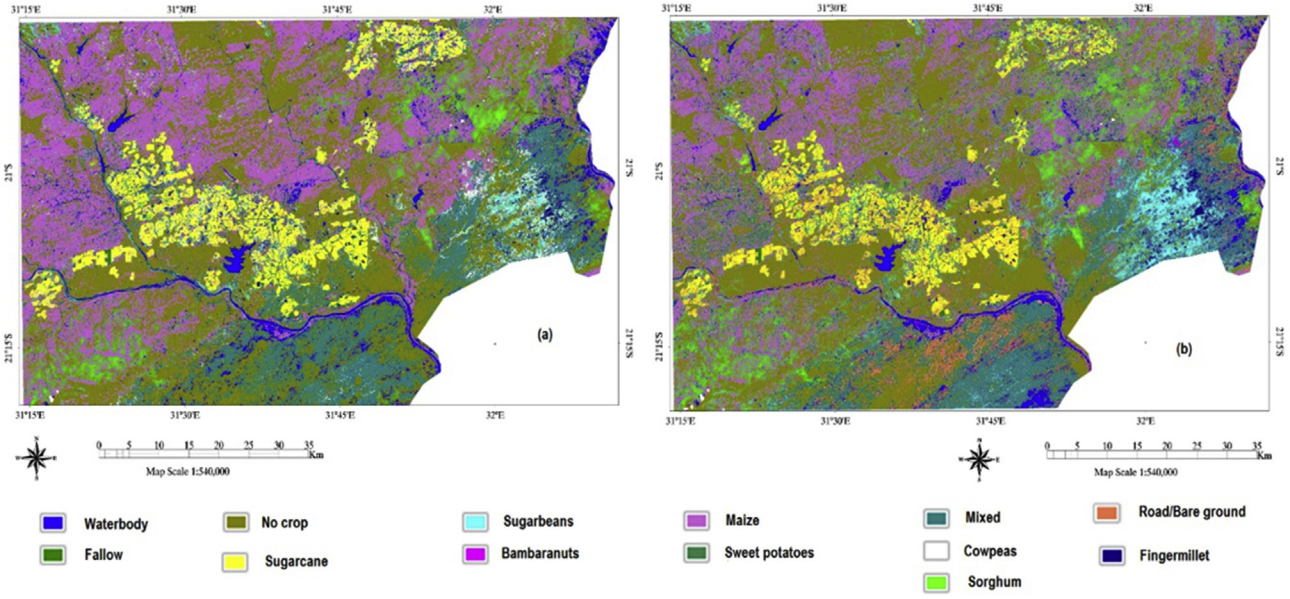

Figure 8. Classified maps (a) Landsat 8 + Sentinel speckle filtered (b) Landsat 8 + Sentinel speckle unfiltered.

Table 3. Z-test statistical significance between Landsat 8 + Sentinel-1 speckle unfiltered and Landsat 8 + Sentinel-1 speckle filtered results at $\alpha = 0.05$.

Scenario	Landsat 8 + Sentinel speckle filtered	Landsat 8 + Sentinel speckle unfiltered
Overall accuracy (%)	94.69%	96.02%
Kappa $\widehat{K}$	0.9378	0.9515
Var ($\widehat{K}$)	0.0076	0.0052
$z = \frac{\lvert\widehat{K}_1 - \widehat{K}_2\rvert}{\sqrt{\sigma^2_{\widehat{K}_1} + \sigma^2_{\widehat{K}_2}}}$	**0.1208**	
Significance:	**Not significantly different**	

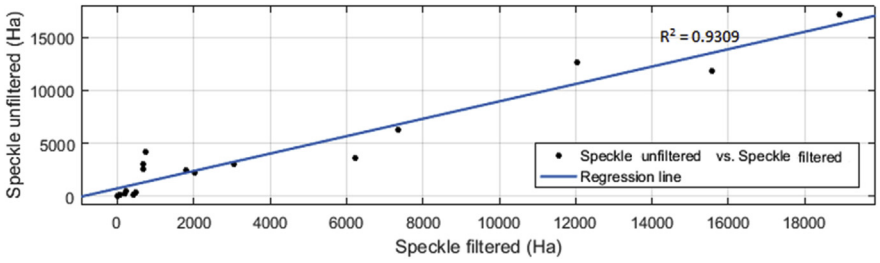

Figure 9. Relationship between crop type areas extracted from the best performing datasets of speckle filtered and speckle unfiltered.

A computed p-value of 0.2715 has been achieved which however is greater than 0.05, therefore the $R^2 = 0.9309$ is statistically significant at 5%. The proposed linear regression model does fit the data sufficiently, hence it is statistically reliable.

4. Discussion

Of all the texture classifiers, GLCM is the most prominently used method by researchers [11], hence making GLCM a power tool for texture analysis. This paper implements a decision-level image fusion of classified maps from Landsat 8 texture features and Sentinel-1 texture features. Window size, input channels, and texture features are employed as the control variables bib48[48, 56]bib56. Generally, textural features have been effective in separating crop types in the area under study.

Texture features derived from red and blue bands are more effective in enhancing crop discrimination and classification capabilities when appended to Landsat 8. Not all texture measures from all bands have a positive effect in enhancing classification. SWIR features have been the least effective since the highest overall accuracy obtained is only 54%, the majority achieved less than 50%. This is one limitation of texture features, there is a need to explore which texture measures are suitable for classification. One swift method to identify appropriate texture features is to apply class separability analysis as proved by Mhangara and Odingi [57]. Nonetheless, the fundamental texture features still require

spectral information to meritoriously enhance the discrimination and classification of crop types.

4.1. Effect of VV and VH polarisation

From the experiment conducted, VH polarization texture features seem to provide more accurate overall classification results compared to VV (Appendix 3). VH polarization backscatter performed better than VV polarization backscatter. The difference is attributed to the fact that the way the microwaves interact with the surface or canopy is also different, and is dependent on the incident angle of the radar pulse on the surface. VH polarimetry has better scattering mechanisms. For VH polarization, vegetation contribution capacity is better than VV polarimetry. VH polarization is more sensitive to the different canopy structures, hence better ability to discriminate different crop types.

The addition of texture features to either VV or VH polarization does not necessarily improve discrimination ability when either of the texture features is classified separately irrespective of the window size used to produce the texture feature or prior application of speckle filtering during pre-processing. Due to the different interactions, the varying VV and VH histograms are also very different. However, the dual polarizations have complementary information which is beneficial in improving classifications. The overall results obtained by dual-polarimetry is greater than either of the single polarimetry. Integration of VV and VH polarizations provide richer crop radar wave scattering information, which effectively improves the crop classification accuracy.

4.2. Effect of speckle filtering on texture features

Exploring whether speckle filtering must be applied when deriving texture feature layers are to be utilized in crop classification. Lee filter is employed in this paper for the reduction of speckle since it is considered to have a limited degradation on the quality of an image, hence maintaining the sharpness of edges, point targets, and linear features. A significant benchmark for texture preservation is arduous to establish since the fine texture is close to the speckle noise level [23]. An ideal speckle filter must be able to preserve lines, edges, point targets, speckle reduction, retention of texture information (spatial variability relating to the scene), and preservation of average values in homogeneous regions.

According to Lee et al. [23], filters with small windows (3×3, or 5×5) perform better when conserving the texture information, but from this research, not applying speckle filtering prior to texture feature extraction produced better results than the speckle filtered texture features. Higher classification accuracy has been achieved by classifying texture features synthesized from unfiltered variables. Lee filter has been adopted as the speckle reduction filter with a window size of 5×5 preserves texture to a lesser extent.

As much as speckles decrease the prospects of visual interpretation and analysis of the scene under, for this research not filtering the SAR imagery before texture feature synthesis enhances the texture derivation, speckle filtering has resulted in some loss of information, the texture is preserved to a lesser extent. Dutra & Sant'Anna [58] argued that there is no widely accepted mathematical definition, which comprises all types of texture that can be found in nature. This may be valued since nature comprises of a complex textural phenomenon. They also claimed that traditional texture measures, such as co-occurrence matrix, derived features and structural approaches have failed to produce a satisfactory characterization of texture in SAR images due to the strong influence of the speckle noise. On the contrary, higher classification accuracy can be attained by classifying texture features synthesized from unfiltered [59, 60]. This research obtained relatively improved overall classification results when GLCM texture features are implemented, though not all texture features enhance discrimination. Probably due to the difference in the environments, the scatterers present, not all texture information can be captured. Authors, however, recommend further exploration of such textures feature analysis areas with different land cover and land use types which include urban cities where there is a built-up land cover, also in mountainous areas. Different filter window sizes can be varied as well to determine the extent to which the filters preserve textural information.

4.3. Effect of window size on texture feature determination

Choosing optimal parameters for texture feature extraction is crucial. This paper implements window sizes; 5×5, 7×7, 9×9, and 11×11 to synthesize seven texture features per band/channel and evaluates the performance of the texture features by the varying window sizes in discrimination and classification of crops. Observations reveal that the smaller the window size, the lower the classification accuracy. Zakeri et al. [49] implemented texture and land cover classification of Tehran city in Iran using SAR imagery. Their results also revealed the same pattern that the smaller the window size, the lower the classification accuracy hence consistency with our observations. Nevertheless, window size varies depending on the environment and application at hand.

Smaller window sizes produce noisy texture feature images, the bigger the window size, the smoother the texture feature image. It is also crucial to understand that the sharpness with which a feature is captured can be minimized as a result of smoothening, that should be avoided beyond certain limits. A large window size though may take time for calculating probabilities in GLCM, since it contains more information [11] than smaller window sizes.

4.4. Decision-level image fusion

The amassed accessibility of satellite optical and radar imagery from multiple sensors enables their fusion can be a challenge but is valuable to data-mine more complementary information from them. GLCM texture features for Landsat 8 and speckle filtered and unfiltered Sentinel-1 backscatter are applied to enhance crop discrimination and classification separately. The best performing texture variable classified maps are integrated by decision level fusion. The advantage of decision-level-based fusion is that it minimizes dataset dimensionality which can be time-consuming, and/or inept that come along with pixel-level and feature-level fusions.

Fused map from speckle unfiltered Sentinel-1 textures and Landsat 8 attained a higher overall accuracy of 96.02%, whereas the speckle filtered fused map obtained 94.96% with kappa coefficients of 0.95 and 0.94 respectively. Landsat 8 and respective texture features can be complemented with Sentinel-1 SAR backscatter and respective texture measures to improve the discrimination and classification performances on crop types.

5. Conclusions

This research is aimed at (i) exploring texture features derived from Landsat 8 OLI and dual-polarized Sentinel-1 SAR both speckle filtered and unfiltered backscatter under varying window sizes; (ii) apply decision-level fusion to aggregate classification results for enhanced crop discrimination; (iii) evaluate the performance of decision-level fused maps. Window sizes 5×5, 7×7, 9×9, and 11×11 are implemented in texture feature extraction. Texture features are created from GLCMs.

Results obtained reveal that texture features derived from VH polarization backscatter performed better than VV polarization backscatter since they attained better overall classification accuracies than VV. Texture information derived from the blue band followed by a red band, speckle unfiltered textures performed better than speckle filtered textures. The top three performers for the three categories have all been derived from 11×11 window size. Decision-level fused images from Landsat and non-speckle filtered maps attained an overall classification accuracy of 96.02%, kappa coefficient of 0.96, and Landsat and speckle filtered achieved 94.69% kappa coefficient of 0.94. The corresponding kappa coefficients are statistically tested using Z-test. At $\alpha = 0.05$, both observations are not statistically different.

F1-scores show that speckle unfiltered variables performed better on most individual class than speckle filtered datasets. A coefficient of determination of 0.9309 is obtained from the extracted areas of crop classes discerned on the decision-level fused maps. Furthermore, F-test reveals that there is a statistically significant relationship between the extracted areas.

Therefore, our conclusion is it is possible to integrate Landsat 8 and Sentinel-1 for crop discrimination. Speckle unfiltering before texture feature extraction can have better discrimination ability and aggregation of Landsat 8 variables improves the quality of the classified image. However, speckle filtering or unfaltering maybe optional when classifying, more research regarding the performance of other decision-level fusion approaches is recommended. Also, feature-level and/or pixel-level fusion techniques need more exploration.

Declarations

Author contribution Statement

Shengbo Chen, Juliana Useya: Conceived and designed the experiments; Performed the experiments; Analyzed and interpreted the data; Wrote the paper.

Hillary Mugiyo: Analyzed and interpreted the data; Contributed reagents, materials, analysis tools or data.

Funding statement

This work was supported by the program for JLU Science and Technology Innovative Research Team (No. 2017TD-26) which is funded by: (1) the Fundamental Research Funds for the Central Universities, China (2) the Plan for Changbai Mountain Scholars of Jilin Province, China (JJLZ[2015]54). (3) Jilin Province and Jilin University co-building project: Application and demonstration of satellite remote sensing in crop planting structure adjustment research (SXGJXX2017-2).

Competing interest statement

The authors declare no conflict of interest.

Additional information

No additional information is available for this paper.

Appendices.

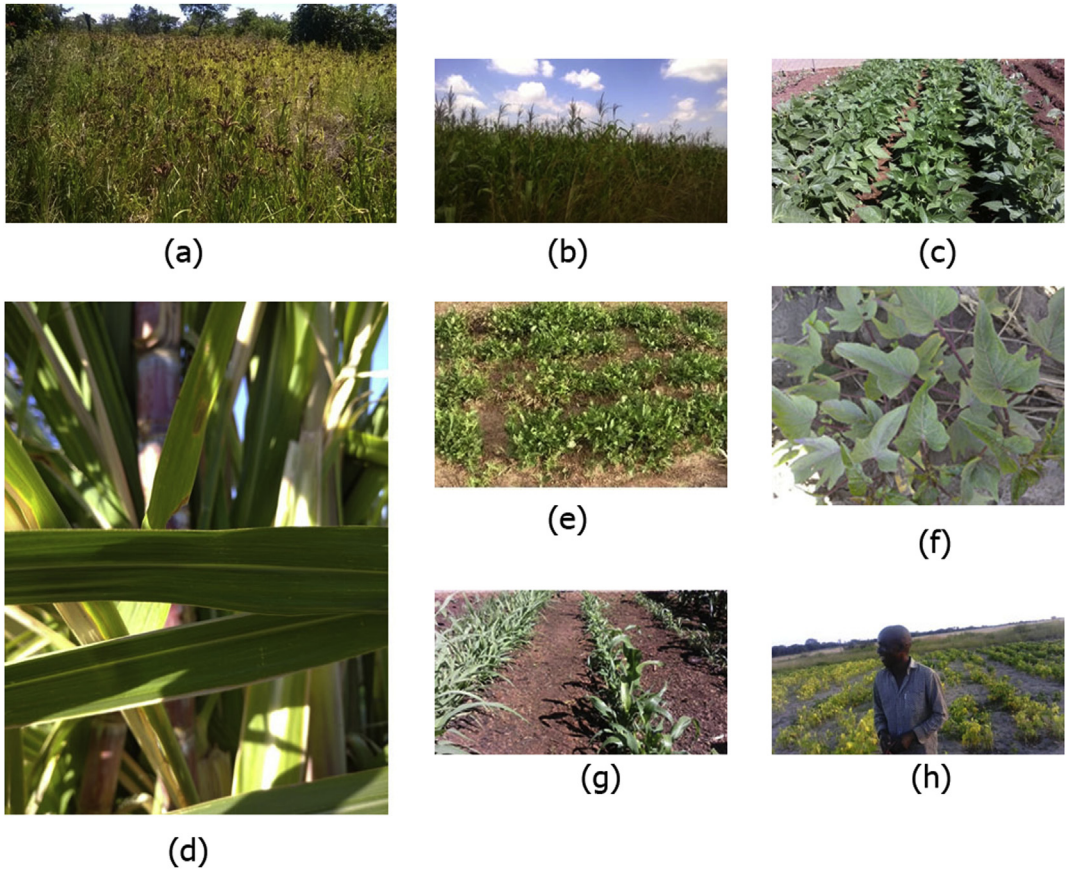

Appendix 1. Sample photos for the sample locations used for the training and validation (a) Finger millet (-21.08°; 32.14°) (b) Maize (-21.08°; 31.56°) (c) Cowpeas (-21.06°; 31.90°) (d) Sugarcane (-21.07°; 31.69°) (e) Bambara nuts (-20.96°; 32.07°) (f) Sweet potato (-21.31°; 31.81°) (g) Sorghum (-21.29°; 31.81°) (h) Sugarbeans (-21.08°; 31.67°).

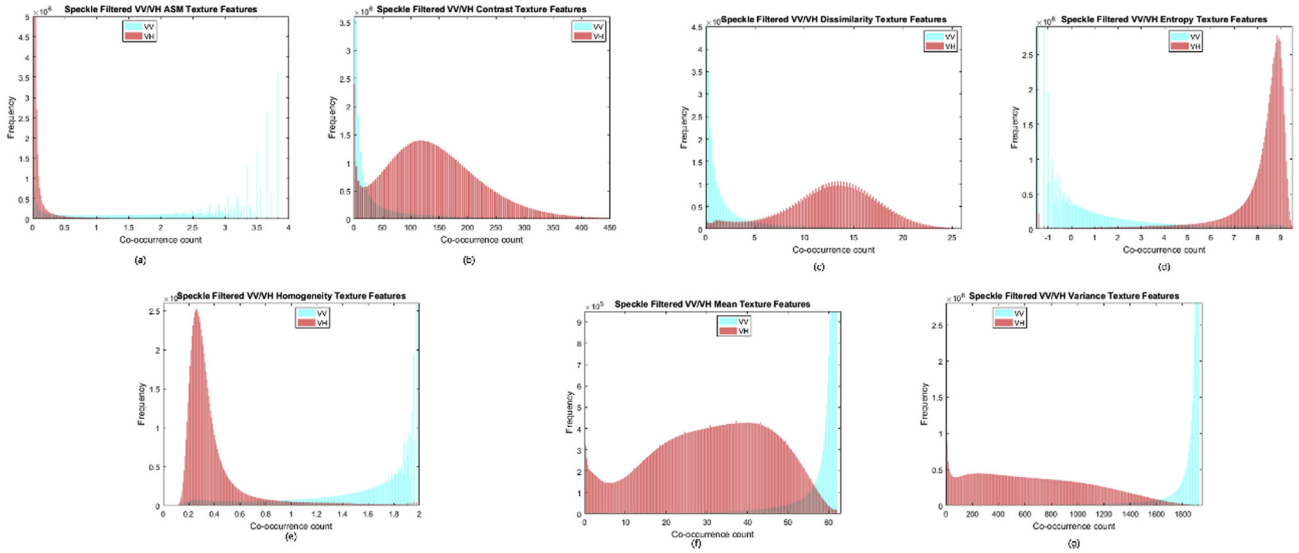

Appendix 2. Histogram intersection for speckle unfiltered VV and VH texture images (a) ASM (b) Contrast (c) Dissimilarity (d) Entropy (f) Homogeneity (f) Mean (g) Variance.

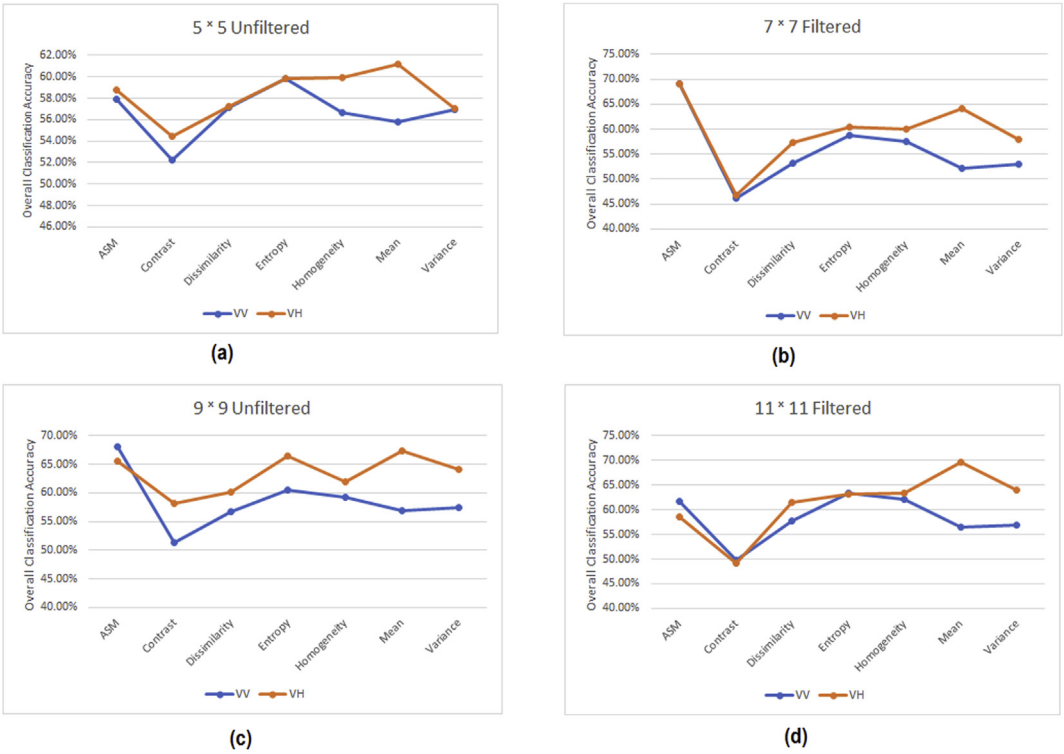

Appendix 3. Single polarized backscatter VV or VH with corresponding texture feature classification accuracies for a selected window sizes (a) 5 × 5 speckle unfiltered (b) 7 × 7 speckle filtered (c) 9 × 9 speckle unfiltered (d) 11 × 11 speckle filtered.

References

[1] J. O'Neil-Dunne, Object-based Approaches to Data Fusion Land Cover Mapping, ASPRS, Sioux Falls Melbourne, Australia, 2017, pp. 2–6 [Online]. Available: http://pecora.asprs.org/.

[2] B.K. Handique, A.Q. Khan, C. Goswami, M. Prashnani, C. Gupta, P.L.N. Raju, Crop discrimination using multispectral sensor onboard unmanned aerial vehicle, Proc. Natl. Acad. Sci. India Sect. A - Phys. Sci. 87 (4) (2017) 713–719.

[3] E.A. Muñoz, A Dissertation on Crops Discrimination Researches Using SAR Data, 2015.

[4] L. Han, et al., Acquisition of paddy rice coverage based on multi-temporal IRS-P6 satellite AWiFS RS-data, Trans. Chin. Soc. Agric. Eng. 23 (3) (2007) 137–143.

[5] J.V. Soares, C.D. Rennó, A.R. Formaggio, C.D.C.F. Yanasse, A.C. Frery, An investigation of the selection of texture features for crop discrimination using SAR imagery, Remote Sens. Environ. 59 (2) (1997) 234–247.

[6] P. Li, S. Fang, SAR image classification based on its texture features, Geo Spatial Inf. Sci. 6 (3) (2003) 16–19.

[7] K.S. Shanmugan, V. Narayanan, V.S. Frost, J.A. Stiles, J.C. Holtzman, Textural features for radar image analysis, IEEE Trans. Geosci. Rem. Sens. GE-19 (3) (1981) 153–156.

[8] V.S. Frost, K.S. Shanmugan, J.C. Holtzman, The influence of sensor and flight parameters on texture in radar images, IEEE Trans. Geosci. Rem. Sens. GE-22 (5) (1984) 440–448.

[9] A.N. Nyoungui, E. Tonye, A. Akono, Evaluation of speckle filtering and texture analysis methods for land cover classification from SAR images, Int. J. Rem. Sens. 23 (9) (2002) 1895–1925.

[10] T. Idol, B. Haack, R. Mahabir, Radar speckle reduction and derived texture measures for land cover/use classification: a case study, Geocarto Int. 32 (1) (2015) 18–29.

[11] A.S. Aghav, P.N.S. Narkhede, Application-oriented approach to texture feature extraction using grey level Co-occurrence matrix (GLCM), Int. J. Eng. Technol. 4 (5) (2017) 3498–3503 [Online]. Available: https://www.irjet.net/archives/V4/i5/IRJET-V4I5844.pdf.

[12] H. Vinciková, M. Hais, J. Brom, J. Procházka, E. Pecharová, Use of remote sensing methods in studying agricultural landscapes – a review, J. Landsc. Stud. 3 (April) (2010) 53–63.

[13] A. Materka, M. Strzelecki, "Texture analysis methods – a review, Methods 11 (1998) 1–33.

[14] R.M. Haralick, K. Shanmugam, I. Dinstein, Textural features for image classification, IEEE Trans. Syst. Man. Cybern. SMC-3 (6) (1973) 610–621.

[15] D. Murashkin, G. Spreen, M. Huntemann, W. Dierking, Method for detection of leads from Sentinel-1 SAR images, Ann. Glaciol. 59 (76pt2) (2018) 124–136.

[16] M. Radovic, M. Djokovic, A. Peulic, N. Filipovic, Application of data mining algorithms for mammogram classification, in: 13th IEEE International Conference on BioInformatics and BioEngineering, 2013, pp. 1–4.

[17] R. Goel, S. Singh, Skin cancer detection using GLCM matrix analysis and back propagation neural network classifier, Int. J. Comput. Appl. 112 (9) (2015) 40–47.

[18] M. Eisa, A.A. Ewees, M.M. Refaat, A. Elgamal, Effective medical image retrieval technique based on texture features, Int. J. Intell. Cooper. Inf. Syst. 13 (2 April) (2013) 19–33.

[19] MathWorks, Texture Analysis Using the Gray-Level Co-occurrence Matrix (GLCM), 2018. https://ww2.mathworks.cn/help/images/texture-analysis-using-the-gray-level-co-occurrence-matrix-glcm.html.

[20] E.A.L. Salas, K.G. Boykin, R. Valdez, Multispectral and texture feature application in image-object analysis of summer vegetation in eastern Tajikistan pamirs, Remote Sens. 8 (1) (2016) 1–20.

[21] A. Ozdarici, Z. Akyurek, A comparison of SAR filtering techniques on agricultural area identification, in: Proceedings of ASPRS 2010 Annual Conference, California, 2010 no. April, pp. 26–30, [Online]. Available: http://www.asprs.org/wp-content/uploads/2013/08/Ozdarici.pdf.

[22] B. Aiazzi, L. Alparone, S. Baronti, M. Bianchini, Information-theoretic textural features of SAR images: an assessment for land cover classification, Image Signal Proc. Rem. Sens. X 5573 (2004) 5511–5573 [Online]. Available:.

[23] J.S. Lee, I. Jurkevich, P. Dewaele, P. Wambacq, A. Oosterlinck, Speckle filtering of synthetic aperture aadar images: a review, Rem. Sens. Rev. 8 (4) (1994) 313–340.

[24] F.T. Ulaby, F. Kouyate, B. Brisco, T.H. Lee Williams, Textural information in SAR images, IEEE Trans. Geosci. Rem. Sens. GE-24 (2) (1986) 235–245.

[25] A. Lopes, E. Nezry, R. Touzi, H. Laur, Structure detection and statistical adaptive speckle filtering in SAR images, Int. J. Rem. Sens. 14 (9) (Jun. 1993) 1735–1758.

[26] M.J. Collins, J. Wiebe, D.A. Clausi, The effect of speckle filtering on scale-dependent texture estimation of a forested scene, IEEE Trans. Geosci. Rem. Sens. 38 (3) (2000) 1160–1170.

[27] Y. Forget, M. Shimoni, M. Gilbert, Complementarity between Sentinel-1 and Landsat 8 Imagery for Built-Up Mapping in Sub-saharan Africa, 2018, pp. 1–13. October.

[28] J. Useya, S. Chen, Comparative performance evaluation of pixel-level and decision-level data fusion of landsat 8 OLI, landsat 7 ETM+ and sentinel-2 MSI for crop ensemble classification, IEEE J. Sel. Top. Appl. Earth Obs. Remote Sens. 11 (11) (2018) 4441–4451.

[29] C.C. Funk, M.E. Brown, Declining global per capita agricultural production and warming oceans threaten food security, Food Secur. 1 (2009) 271–289.

[30] K. Hentze, F. Thonfeld, G. Menz, Evaluating crop area mapping from MODIS time-series as an assessment tool for Zimbabwe ' s ' fast track land reform programme, PloS One (2016) 1–22.

[31] C. Maguranyanga, A. Murwira, Mapping maize, tobacco, and soybean fields in large-scale commercial farms of Zimbabwe based on multitemporal NDVI images in MAXENT, Can. J. Rem. Sens. 40 (6) (2014) 396–405.

[32] C. Maguranyanga, A. Murwira, M. Sibanda, Distinguishing maize, soyabean and tobacco fields using temporal MODIS 16 Day NDVI images in the large scale commercial farming areas of Zimbabwe, J. Indian Soc. Remote Sens. 43 (1) (2015) 79–87.

[33] M. Sibanda, A. Murwira, The use of multi-temporal MODIS images with ground data to distinguish cotton from maize and sorghum fields in smallholder agricultural landscapes of Southern Africa, Int. J. Rem. Sens. 33 (16) (2012) 4841–4855. August.

[34] G. Toringepi, The Contribution of Smallholder Agriculture Production to Food Security in Rural Zimbabwe: A Case Study of Masvingo Province, University of Fort Hare, 2016, pp. 1–139.

[35] S. Abdikan, F.B. Sanli, M. Ustuner, F. Calò, Land cover mapping using sentinel-1 sar data, ISPRS - Int. Arch. Photogramm. Remote Sens. Spat. Inf. Sci. XLI-B7 (July) (2016) 757–761.

[36] G. Suresh, R. Gehrke, T. Wiatr, M. Hovenbitzer, Synthetic aperture radar (SAR) based classifiers for land applications in Germany, Int. Arch. Photogr. Rem. Sens. Spat. Inf. Sci. ISPRS Arch. XLI-B1 (July) (2016) 1187–1193.

[37] G. Wang, W. Zi, C. Xie, F. Zhang, Dual-aspect geometric and radiometric terrain correction method for high-resolution SARA data, in: IEEE International Geoscience and Remote Sensing Symposium, 2011, pp. 1894–1897.

[38] C. Wen, Y. Zhang, K. Deng, Urban area classification in high resolution SAR based on texture features, in: International Conference on Geo-Spatial Solutions for Emergency Management and the 50th Anniversary of the Chinese Academy of Surveying and Mapping, 2011, pp. 281–285 [Online]. Available: http://www.isprs.org/proceedings/XXXVIII/7-C4/281_GSEM2009.pdf.

[39] P. Mohanaiah, P. Sathyanarayana, L. Gurukumar, Image texture feature extraction using GLCM approach, Int. J. Sci. Res. Publ. 3 (5) (2013) 1–5.

[40] M. Hall-Beyer, GLCM texture: a tutorial, Natl. Counc. Geogr. Inf. Anal. Remote Sens. Core Curric. 3 (2000) 1–12.

[41] D.M. Lane, M. Hebl, D. Osherson, H. Ziemer, "Histograms," *Online Statistical Book*, 2018. http://onlinestatbook.com/2/graphing_distributions/histograms.html.

[42] W. Yang, L. Xu, X. Chen, F. Zheng, Y. Liu, Chi-squared distance metric learning for histogram data, Math. Probl Eng. (2015) 1–12.

[43] S.I. Bityukov, A.V. Maksimushkina, V.V. Smirnova, Comparison of histograms in physical research, Nucl. Energy Technol. 2 (2) (2016) 108–113.

[44] T. Ahonen, A. Hadid, M. Pietikainen, Face description with local binary patterns: application to face recognition, IEEE Trans. Pattern Anal. Mach. Intell. 28 (12) (2006) 2037–2041.

[45] P. Mantero, G. Moser, S.B. Serpico, Partially supervised classification of remote sensing images through SVM-based probability density estimation, IEEE Trans. Geosci. Rem. Sens. 43 (3) (2005) 559–570.

[46] G. Mountrakis, J. Im, C. Ogole, Support vector machines in remote sensing: a review, ISPRS J. Photogrammetry Remote Sens. 66 (3) (2011) 247–259.

[47] B.E. Boser, I.M. Guyon, V.N. Vapnik, A training algorithm for optimal margin classifers, in: Proceedings of the 5th Annual Workshop on Computational Learning Theory, 1992, pp. 144–152.

[48] T. He, Y.-J. Sun, J.-D. Xu, X.-J. Wang, C.-R. Hu, Enhanced land use/cover classification using support vector machines and fuzzy k-means clustering algorithms, J. Appl. Remote Sens. 8 (2014).

[49] H. Zakeri, F. Yamazaki, W. Liu, Texture analysis and land cover classification of tehran using polarimetric synthetic aperture radar imagery, Appl. Sci. MDPI 7 (5) (2017) 452.

[50] H. Studley, K. Weber, Comparison of Image Resampling Techniques for Satellite Imagery, 2011.

[51] J.A. Parker, R.V. Kenyon, D.E. Troxel, Comparison of interpolating methods for image resampling, IEEE Trans. Med. Imag. 2 (1) (1983) 31–39.

[52] D.G. Rossiter, Technical Note: Statistical Methods for Accuracy Assessment of Classified Thematic Maps, Enschede The Netherlands, 2004 [Online]. Available: https://www.researchgate.net/publication/228802780_Technical_Note_Statistical_methods_for_accuracy_assesment_of_classified_thematic_maps.

[53] D. Brzezinski, J. Stefanowski, Prequential AUC: properties of the area under the ROC curve for data streams with concept drift, Knowl. Inf. Syst. 52 (2) (2017) 531–562.

[54] T. Tshabalala, B. Ncube, H.P. Moyo, E.M. Abdel-Rahman, O. Mutanga, A.R. Ndhlala, Predicting the spatial suitability distribution of Moringa oleifera cultivation using analytical hierarchical process modelling, South Afr. J. Bot. 129 (2020) 161–168.

[55] K. Jia, et al., Land cover classification of landsat data with phenological features extracted from time series MODIS NDVI data, Rem. Sens. 6 (11) (2014) 11518–11532.

[56] H. Wang, Y. Zhao, R. Pu, Z. Zhang, Mapping robinia pseudoacacia forest health conditions by using combined spectral, spatial, and textural information extracted from IKONOS imagery and random forest classifier, Rem. Sens. 7 (7) (2015) 9020–9044.

[57] P. Mhangara, J. Odindi, Potential of texture-based classification in urban landscapes using multispectral aerial photos, S. Afr. J. Sci. 109 (3–4) (2013) 1–8.

[58] L.V. Dutra, S.J.S. Sant'Anna, The effect of speckle filtering on SAR texture discrimination, in: Anais VIII Simpósio Brasileiro de Sensoriamento Remoto, 1996, pp. 839–843.

[59] Q. Song, et al., In-season crop mapping with GF-1WFV data by combining object-based image analysis and random forest, Remote Sens. MDPI 9 (11) (2017) 1184.

[60] Y. Zhang, S. Wang, G. Ji, P. Phillips, Fruit classification using computer vision and feedforward neural network, J. Food Eng. 143 (2014) 167–177.